Experimental characterization of dielectric-loaded plasmonic waveguide-racetrack resonators at near-infrared wavelengths

C. Garcia[1,2,*], V. Coello[3], Z. Han[2,4], I. P. Radko[2] and S. I. Bozhevolnyi [2]

[1] *Doctorado en Ingeniería Física Industrial, Universidad Autónoma de Nuevo León, Ave. Universidad s/n. Cd. Universitaria, San Nicolás de los Garza, N.L. México, C.P. 66450.*

[2] *Institute of Technology and Innovation (ITI), University of Southern Denmark, Niels Bohrs Allé 1, DK-5230 Odense M, Denmark.*

[3] *Centro de Investigación Científica y Educación Superior de Ensenada, Unidad Monterrey, Km 9.5 Carretera Nueva al Aeropuerto. PIIT. Apodaca, N.L. México, C.P.66600.*

[4] *Center for THz Research, China Jiliang University, Hangzhou 310018, China.*

[*] Corresponding author: cegarcia@cicese.mx. Tel. (+52)8114935550 Ext. 2036

Abstract

Dielectric-loaded plasmonic waveguide-racetrack resonators (WRTRs) were designed and fabricated for operating at near-infrared wavelengths (750-850nm) and characterized using leakage radiation microscopy. The transmission spectra of WRTRs are found experimentally and compared to the calculated analytical expression. The wavelength-dependent parameters of the analytical expression, i.e. the propagation length and effective index dispersion, were also estimated experimentally by leakage radiation imaging of direct and Fourier space, respectively. The fabricated structures exhibited high extinction ratio (~20dB) and good agreement between calculated and measured transmission values.

1. Introduction

In the last years, plasmonics has become an intensive research area due to its potential applications in biosensing [1], inter-chip and intra-chip applications in computer systems, data storage and communications [2, 3]. Plasmonics offers the opportunity to combine optical functionality in the same physical area as existing electronic devices by exploiting the unique optical properties of surface plasmon polaritons (SPPs). SPPs are quasi-two dimensional electromagnetic waves of electron excitations, propagating at a metal-dielectric interface and having field components decaying exponentially into both neighboring media [4]. Unlike

electronics, plasmonic devices grant much faster response time (~10^{14} Hertz) and also broader bandwidths [5]. Several plasmonic devices have already been investigated, such as refractive elements [6], interferometers [7] parabolic mirrors [8], band-gap structures [9] and waveguides [10-14] among others. Research on SPP wave-guiding has been of utmost importance since it is essential for controlled plasmonic manipulation. Plasmonic waveguides are used to guide SPP modes and can be configured by using different geometries and materials. In this context, metallic photonic crystals, thin metal strips, metal nanoparticle chains and metal nanorods have been introduced as SPP guiding mechanisms [10]. However, in these structures, the field is weekly localized in the transverse section. Dielectric-loaded SPP waveguides (DLSPPWs) represent an attractive alternative to improve the SPP-mode lateral confinement. DLSPPWs are special kind of waveguides where a high-index contrast (core refractive index much different from the neighboring media) is used to shrink the mode size by strongly confining the SPP field in the transverse section. Nevertheless, with better confinement, the lower the propagation length. This trade-off between localization and propagation is one of the main issues in SPP guiding. DLSPPWs were theoretically investigated [11] using the effective index method [15] and the finite element method. Recently, the potential of DLSPPWs based components for wavelength selection was also explored [12]. The investigation included waveguide-ring resonators (WRRs) and in-line Bragg gratings at the telecommunication wavelength range. Other studies showed waveguide-racetrack resonators (WRTRs) to be an attractive alternative besides WRRs [16, 17]. The larger coupling region of WRTRs yields flexibility in fabrication parameters, hence relaxing the requirements of fabrication resolution. It is, however, difficult to foresee the WRTR behavior within other important wavelength ranges, e.g. at near-infrared accessible with Ti:Sapphire lasers, because all the important properties (propagation length, mode confinement and effective index dispersion) are expected to be significantly different. . In this work, we report on the design, fabrication and characterization of dielectric-loaded plasmonic WRTRs at near-infrared wavelengths, which is the first investigation in this wavelength range. WRTRs transmission spectra are measured using leakage radiation microscopy (LRM) and compared to the calculated analytical values. High extinction ratios (~20dB) are achieved compared to those obtained in previous results with WRRs at telecommunication range (~13dB) [12, 13]. The propagation length and effective index dispersion are also measured by recording the leakage radiation at the direct and Fourier space respectively. This paper is organized as follows. Section 2 describes the sample fabrication process and the experimental setup. Experimental results and discussion are presented in section 3. Finally, in section 4 conclusions are shown.

2. Materials and Methods

The structures were fabricated using electron-beam lithography. The DLSPPW consists of a strip of poly-methyl-methacrylate (PMMA) deposited, by using spin-coating process, on a 70nm gold film (Fig. 1a). Based in previously published results [11], both width w and thicknesses t were chosen to be 300nm in order to impose mono-modal conditions. The WRTRs considered in this work consist of a straight waveguide (bus-waveguide) in close proximity to a racetrack-shaped waveguide structure (Fig. 1b). Therefore, the propagated light can be coupled, from one waveguide to another, through evanescent wave coupling. The bus-waveguide includes a taper, at one of its ends, that is used to couple light efficiently into SPP waveguide mode by directly illuminating the taper region with a moderately focused laser beam. Due to the scattering of light on the nanostructure, various components of the wave-vector are produced with one of them necessary matching the wave-vector of the waveguided mode (the DLSPPW mode), hereby providing its excitation.
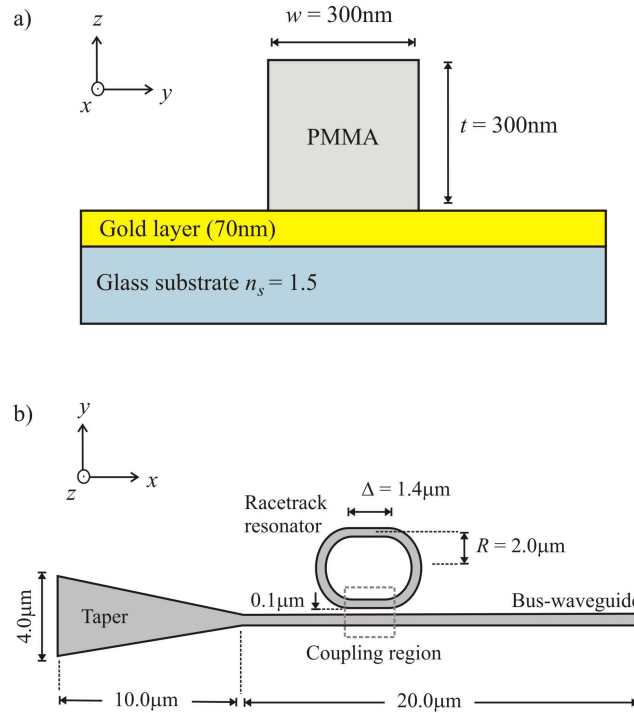

Fig. 1. (a) Schematic diagram of the transverse section of a DLSPPW. (b) SPP waveguide racetrack resonator. The width w and thickness t of the WRTR is the same as shown in (a).

WRTRs differ from WRRs in that they have a straight interaction section which runs parallel with the waveguide, therefore elongating the interaction region. The fabricated racetrack resonator has two straight sections of length $\Delta = 1.4\mu m$. The main motivation of using racetrack resonators is that one can increase the waveguide-resonator separation for a desired coupling

ratio, hence relaxing the resolution requirements of fabrication [16]. Other studies have also demonstrated that racetrack resonators exhibit a significant improvement in the extinction ratio due to the larger coupling region [17]. The gap, g, between the bus-waveguide and the resonator, is ~100nm and the racetrack resonator radius, R, is ~2.0μm. Additionally, straight waveguides, with the same parameters as the bus-waveguide described above, were fabricated in order to calculate the waveguide propagation lengths and effective indexes. WRTR transmission spectrum and the DLSPPWs mode characteristics are both measured using LRM, where a tunable Ti:Sapphire laser is used as the illumination source. The experimental setup is described in detail elsewhere [14]. LRM technique provides the possibility to image, both, direct and Fourier planes and therefore allows one to obtain information about propagation length and effective index respectively.

3. Experimental results

3.1 Propagation length

The power propagation length, L_{SP}, of the DLSPPW mode was measured by taking averaged cross sectional profiles from the LRM image of the straight waveguide where the SPP mode is clearly guided (Fig. 2a). The intensity spatial distribution of the SPP can be written as $I(x) = I(y_0, z_0) \exp(-2\beta''x)$, where β'' is the imaginary part of the propagation constant ($\beta = \beta' + i\beta''$), and is related to the propagation length by $L_{SP} = 1/(2\beta'')$. The resulting SPP intensity distribution (Fig. 2b), obtained from the LRM image at an illumination wavelength of 760nm, clearly shows that the SPP intensity decays exponentially along the propagation direction (x-direction). Quite noticeable oscillations of the intensity along the profile are common in LRM technique and arise from interference of the main LRM signal with close spatial components, such as those leaking from a mode in the funnel region, which has slightly different effective index due to the wider dielectric boundaries.
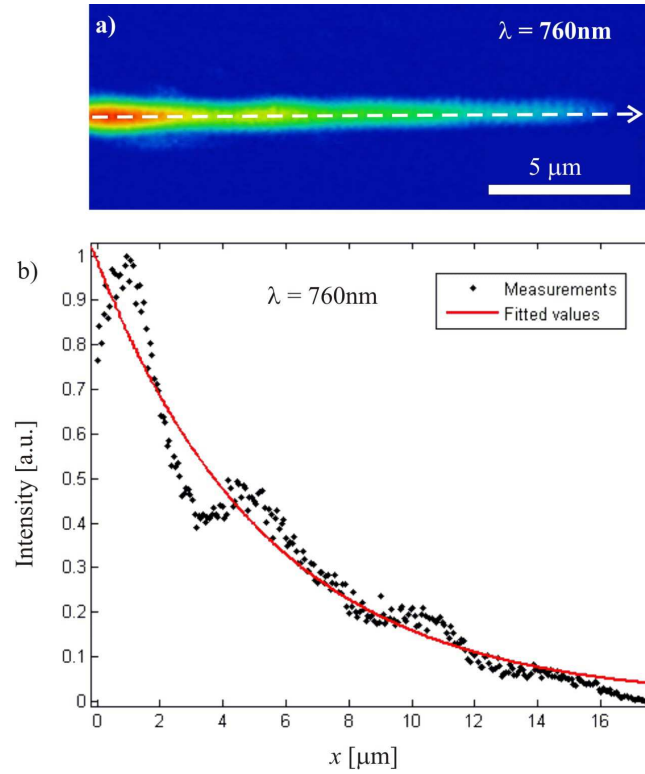
Fig. 2. (a) LRM image of a straight DLSPPW illuminated with a free-space excitation wavelength of 760nm. (b) Averaged intensity profile along the cross section shown in (a) and fitted curve.

By using the best fit for the experimental data, we find a propagation length of ~4.7μm. The procedure is repeated for different wavelengths (760-820nm) and, since data follows a linear behavior in this range (Fig. 3), we get a linear fit of the form:

$$L_{SP}(\lambda) = -3.08 + 10.8\lambda \text{(μm)}. \tag{1}$$

The propagation length variation for this configuration is minimal (<1μm) in this range. This allows the possibility of choosing a constant value for L_{SP} with no significant differences when calculating the transmission spectra of WRTRs. For our purposes we use the complete expression of Eq. 1.
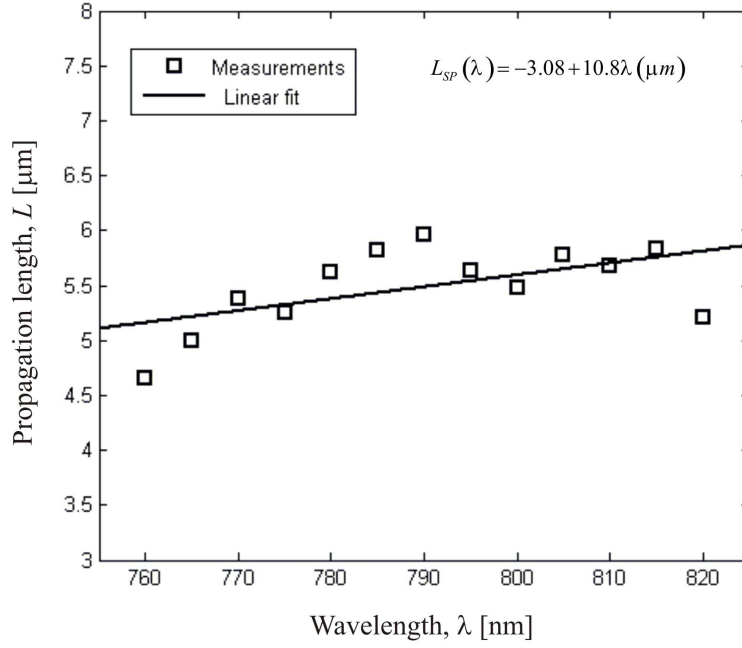
Fig. 3. Propagation lengths and linear fit associated to a straight DLSPPW at different excitation wavelengths in the interval 760-820nm.

3.2 Effective Index

In section 3.1, the leakage radiation was recorded in the image plane in order to measure the SPP propagation length. However, leakage radiation imaging is also possible in the Fourier plane of the LRM, e.g. imaging the SPP wavevector space. The real part of the propagation constant, β' is related to the mode effective index according to $\beta' = k_0 n_{eff}$. It is clear that an experimental determination of the mode effective index implies measurements in the Fourier plane. The leakage radiation recorded in the Fourier plane of the microscope when a SPP guided mode is propagating in a straight DLSPPW (Fig. 4a) exhibit information regarding the effective index of the guided mode and also from the numerical apertures of the objectives used in the experimental setup. The inner disc (Fig. 4a) corresponds to the focusing microscope objective used for the SPP excitation (NA = 0.40). The two crescents, which also indicate the polarization direction [18], are characteristic of the Au/Air SPP mode (n_{eff} ~1.01). The vertical line, which corresponds to the value of the propagation constant, is the signature of a SPP guided mode that propagates in the positive x direction in the DLSPPW. Finally, there is also an outermost disc that corresponds to the collecting objective high numerical aperture (NA = 1.45). The leakage radiation image recorded by the CCD camera in the Fourier plane (Fig. 4b) shows these elements clearly, which are used for calibration and for the experimental determination of the effective index of the mode. The distance from the origin to the crescent is used to calibrate the
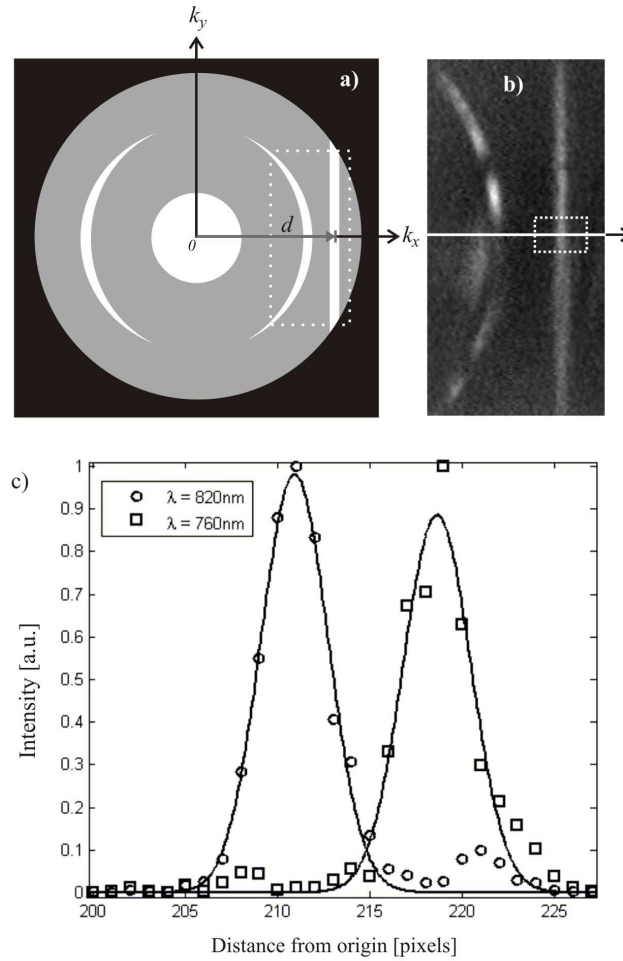
Fig. 4. (a) Fourier plane schematic showing the interest region, where d is the distance from the origin to the straight line that corresponds to the guided mode signature. (b) LRM cropped image of the Fourier plane. (c) Cross sectional profiles for two different wavelengths (760 and 820nm) and Lorentzian fit.

Fourier plane by finding a scale factor that relates the distance in pixels with a known effective index. The value of the mode effective index can be then calculated by measuring the distance in pixels from the origin to the central position of the mode signature (straight line) and applying the factor scale. The distance is measured by analyzing averaged cross sections along d (Fig. 4c). It should be noticed that the horizontal axis of the graph in Fig. 4c does not start at the origin, but instead, only the interest section appears (dotted line rectangle of Fig. 4b). The difference in the central position of the straight line between different wavelengths is very small and introduces high uncertainty to distinguish one from another. To solve this problem the intensity profiles are fitted to a Lorentzian curve to find a more accurate center position. A shift in the position d of the guided mode signature is clearly seen.

The abovementioned procedure is repeated in the wavelength interval 760-820nm to calculate the effective index dispersion in this range (Fig. 5). Also in this case a linear fit is suitable and the following expression is obtained

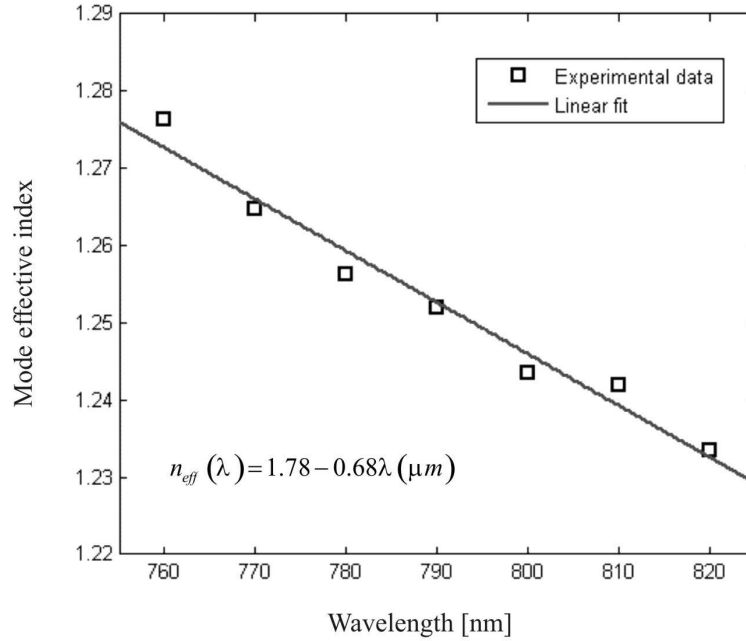$$n_{eff}(\lambda) = 1.78 - 0.68\lambda(\mu m). \tag{2}$$

Fig. 5. Experimental data and linear fit of the mode effective index dispersion measured in the wavelength interval of 760-820nm for a straight DLSPPW.

3.3 WRTR transmission

Only certain wavelengths can build up in intensity in a racetrack resonator. The resonance condition occurs when the round-trip optical path length is equal to an integral number of wavelengths. This feature makes WRTRs suitable to act as wavelength selective filters. The transmission analytical expression of WRRs is given by [19]

$$T = \exp\left(\frac{-l}{L_{SP}(\lambda)}\right) \frac{\alpha^2 + t^2 - 2\alpha t \cos\theta}{1 + \alpha^2 t^2 - 2\alpha t \cos\theta}. \tag{3}$$

The first factor of Eq. 3 corresponds to the exponential decay of the SPP, where l is the distance from A to B (Fig. 6a). $\alpha = \exp(-C\beta'')\sigma$ is a parameter accounting for the field attenuation per roundtrip around the resonator, where σ is the pure bend loss factor and $C = 2\pi R + 2\Delta$ is the

circumference of the racetrack resonator. t is the field transmission and represents the coupling losses in the interaction region. The phase change around the resonator is $\theta = (2\pi/\lambda)n_{eff}(\lambda)C$, where λ is the free-space wavelength. The values for the power propagation length L_{SP} and the effective index n_{eff} are taken from the results obtained on sections (3.1) and (3.2). The circumference C, the bend loss factor σ and the field transmission t are calculated through numerical fitting. WRTRs transmission spectrum was measured experimentally by analyzing the LRM image (Fig. 6b).
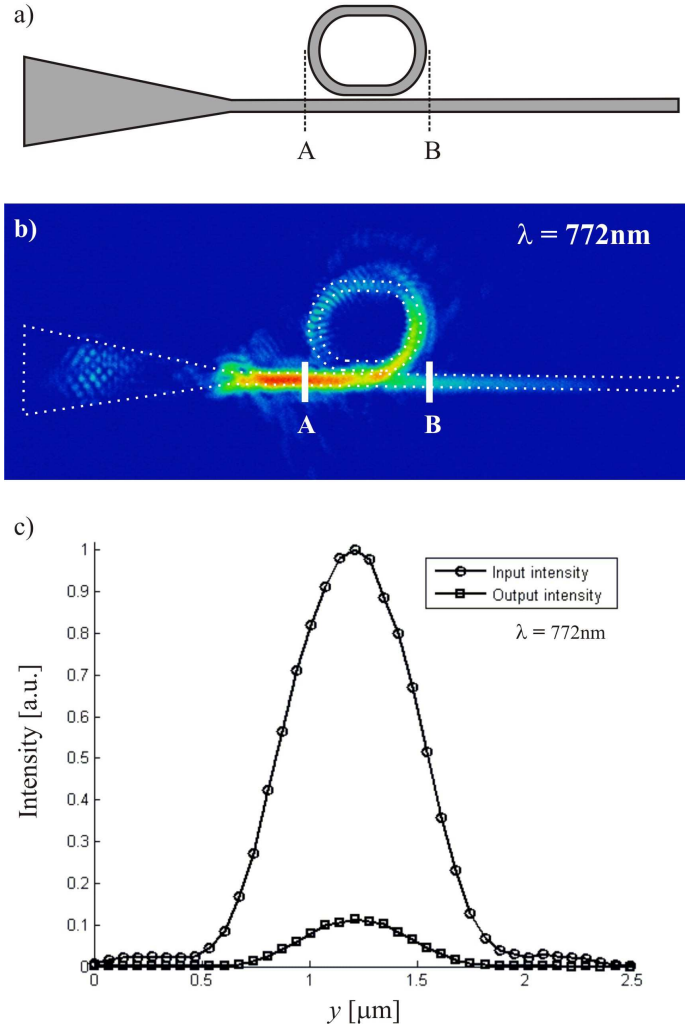

Fig. 6. (a) WRTR structure. (b) LRM image of a WRTR illuminated with a free-space wavelength of 772nm. The structure is highlighted with intermittent lines on (b). (c) Cross sectional intensity profiles along A (Input intensity) and B (Output intensity) of the LRM image in (b).

The input and output intensity, located at point A and B, respectively, are found by obtaining the averaged intensity profiles at these points (Fig. 6c). The fabricated structures were exposed to different dose factors in order to get slight variations of the WRTRs dimensions. Changing the dose factor modifies the width of the waveguide, and therefore the gap between the bus-waveguide and the resonator can become larger or smaller, hence the coupling will also be

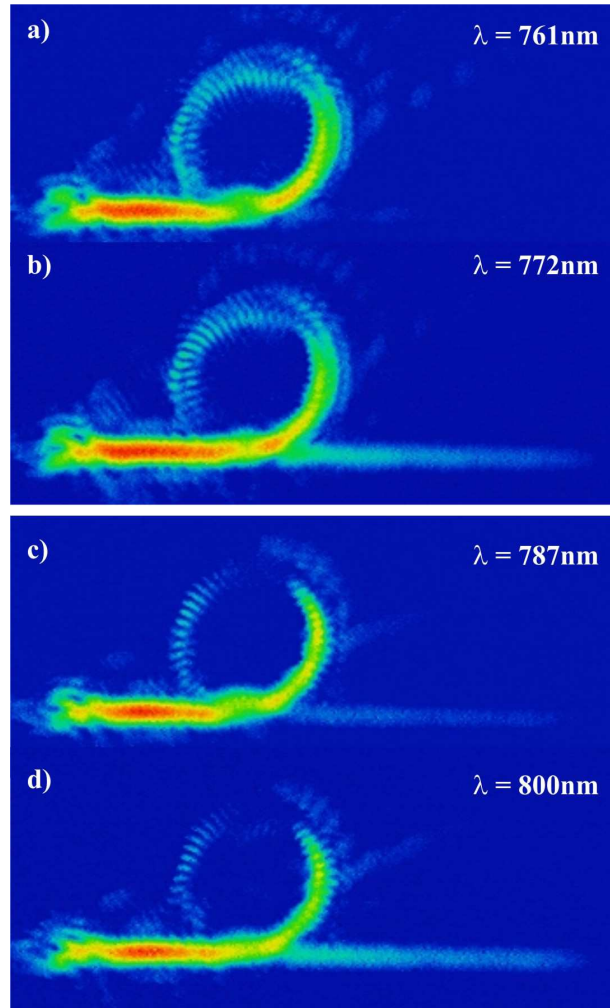affected. LRM images of WRTRs that were exposed to different dose factors were analyzed (Fig. 7).

Fig. 7. LRM images of WRTR structures exposed to different dose factors during fabrication, [(a) and (b)] 0.50 and [(c) and (d)] 0.52. The structures are illuminated at different wavelengths to show minimum and maximum transmission.

With poor coupling WRTRs exhibit low extinction ratio and thereby we choose the structure with the best coupling for further characterization. The WRTR that was fabricated with a dose factor of 0.50 exhibited a high extinction ratio. Transmission minima occur close to $\lambda = 761$ and 784nm (Fig. 8a and c) and maxima around $\lambda = 772$ and 796nm (Fig. 8b and d). The experimental measurements of transmission are plotted as a function of wavelength (Fig. 8e). Measured data exhibited a bandwidth of ~11nm and a high extinction ratio of ~20dB which, so far, is the largest ratio reported for plasmonic wavelength-selective filters. The measured and calculated values of the WRTR transmission (Fig. 8e) are processed numerically to find the best fit. The fitted values are $C = 15.09 \pm 0.01\mu m$, $\sigma = 1.0 \pm 0.2$ and $t = 0.32 \pm 0.04$ (the uncertainty intervals account for 95% of confidence). α is also calculated giving values from 0.22 to 0.25,

due to its wavelength dependence. The fitted value of the resonator circumference C differs only by ~300nm (< 2%) from the original fabrication parameters and the fitted value of σ, very close to unity, corresponds to very low bend losses.
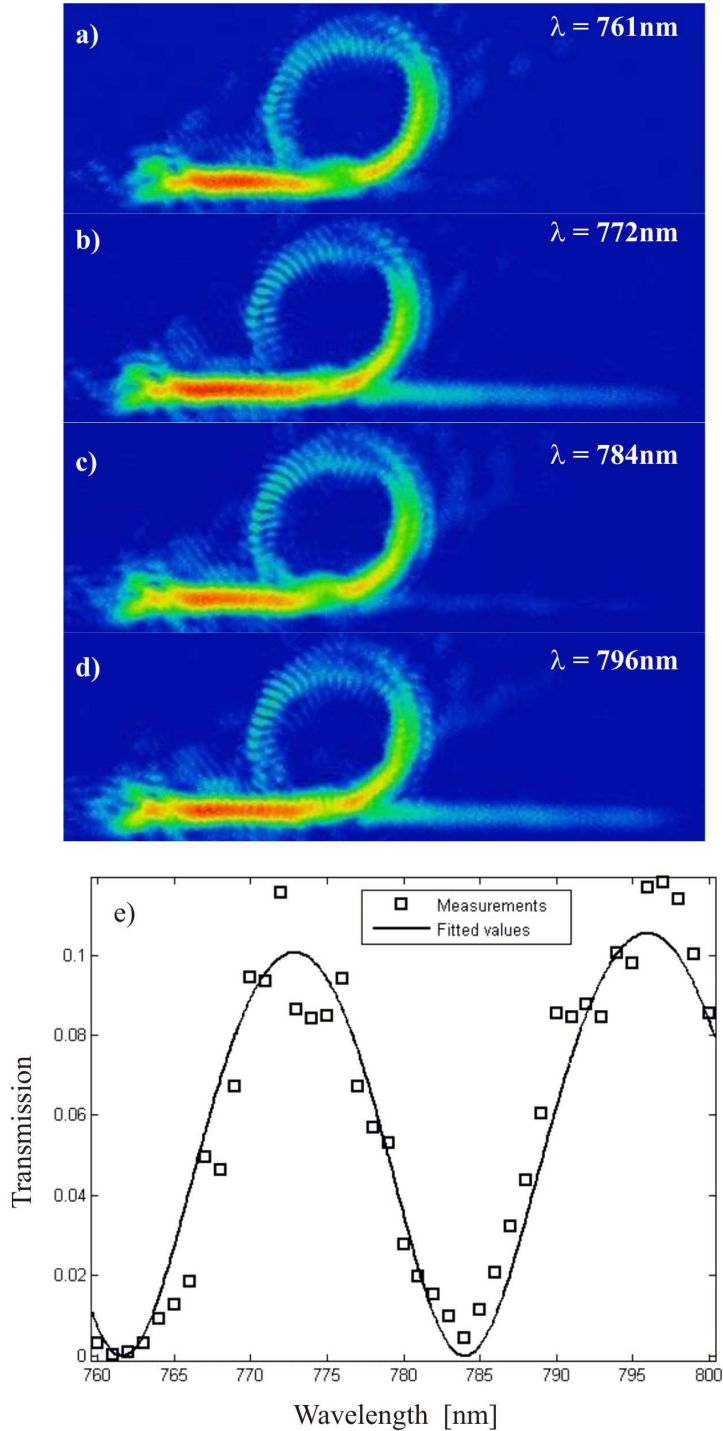

Fig. 8. [(a)-(d)] WRTR LRM images illuminated with the free-space wavelength of (a) 761nm, (b) 772nm, (c) 784nm and (d) 796nm. (e) WRTR transmission spectrum. Experimental measurements where obtained from LRM image analysis and the fitted values are found from the analytical expression.

4 Conclusions

The fabricated WRTRs exhibited high extinction ratio, good mode confinement and relatively low losses and thus the feasibility for using these structures in the near-infrared wavelength range was demonstrated. Moreover, the extinction ratio we report is the largest achieved, so far, on similar plasmonic devices. However, the maximum measured transmission values showed to be quite low (~0.1). Some ways to improve the transmission could be by changing the resonator position and moving it closer to the taper, decreasing the size (R, Δ or both) or using longer wavelengths accessible with Ti:Sapphire lasers (e.g. ~850nm). The use of LRM admits the possibility of imaging both direct and Fourier space, hence allowing measurements of the propagation length and effective index (in contrast with scanning near-field optical microscopes where only propagation length can be calculated). Good agreement is found between measured WRTR transmission values and the obtained semi-analytical fit. This fact indicates that it is possible to calculate the dispersion relation of a DLSPPW mode, as an alternative besides numerical simulations, from experimental measurements and use them for describing the performance of a WRTR. This method offers a more accurate result than those obtained numerically since simulations account for perfectly constructed waveguides, a situation that is very hard to accomplish with electron-beam lithography. When dispersion relations are obtained experimentally the real physical parameters and fabrication defects are intrinsically considered. Furthermore, there is no need of measuring the waveguide dimensions (width and thickness) after fabrication. One should point out, however, that DLSPPW modes with higher effective index than the NA of the collecting objective from the LRM setup cannot be detected.

Acknowledgements

References

1. J. N. Anker, W. P. Hall, O. Lyandres, N. C. Shah, J. Zhao, R.P. Van Duyne: Nature Mater. **7**, 442-453 (2008)

2. A. A. Sawchuck: Proc. IEEE **72**, 758-779 (1984)

3. A. Huang: Proc. IEEE **72**, 780-786 (1984)

4. H. Raether: 1st ed. (Springer-Verlag, Berlin, 1988)

5. K. F. MacDonald, Z. L. Samson, M. I. Stockman and N. I. Zheludev: Nature Photon. **3**, 55-58 (2009)

6. I. P. Radko, A. B. Evlyukhin, A. Boltasseva and S. I. Bozhevolnyi: Opt. Express **16**, 3924-3930 (2008)

7. V. Coello, T. Søndergaard, S. I. Bozhevolnyi: Opt. Commun. **240**, 345–350 (2004)

8. I. P. Radko, S. I. Bozhevolnyi, A. B. Evlyukhin, and A. Boltasseva: Opt. Express **15**, 6576-6582 (2007)

9. S. I. Bozhevolny, J. Erland, K. Leosson, P. M. W. Skovgaard and J. M. Hvam: Phys.Rev.Lett. **86**, 3008-3011 (2001)

10. S. A. Maier, H. A. Atwater: J. Appl. Phys. **98**, 011101 (2005)

11. T. Holmgaard and S. I. Bozhevolnyi: Phys. Rev. B **75**, 245405 (2007)

12 T. Holmgaard, Z. Chen, S. I. Bozhevolnyi, L. Markey, A. Dereux, A. V. Krasavin and A. V. Zayats: Appl. Phys. Lett. **94**, 051111 (2009)

13. T. Holmgaard, Z. Chen, S.I. Bozhevolnyi, L. Markey and A. Dereux: Opt. Express **17**, 2968-2975 (2009)

14. J. Grandidier, S. Massenot, G. Colas des Francs, A. Bouhelier, J.-C. Weeber, L. Markey, and A. Dereux, J. Renger, M. U. González, and R. Quidant: Phys. Rev. B **78**, 245419 (2008)

15. G. B. Hocker and W. K. Burns: Appl. Opt. **16**, 113 (1977)

16. A. Seidel, C. Reinhardt, T. Holmgaard, W. Cheng, T. Rosenzveig, K. Leosson, S. I. Bozhevolnyi, B. N. Chichkov: IEEE Photon. J. **2**, 652-658 (2010)

17. Z. Han: Photo. Nano. Fund. Appl. **8**, 172–176 (2010)

18. B. Hecht, H. Bielefeldt, L. Novotny, Y. Inouye, and D. W. Pohl: Phys. Rev. Lett. **77**, 1889 (1996)

19. A. Yariv: Electron. Lett. **36**, 321-322 (2000)